## Figure 2.1

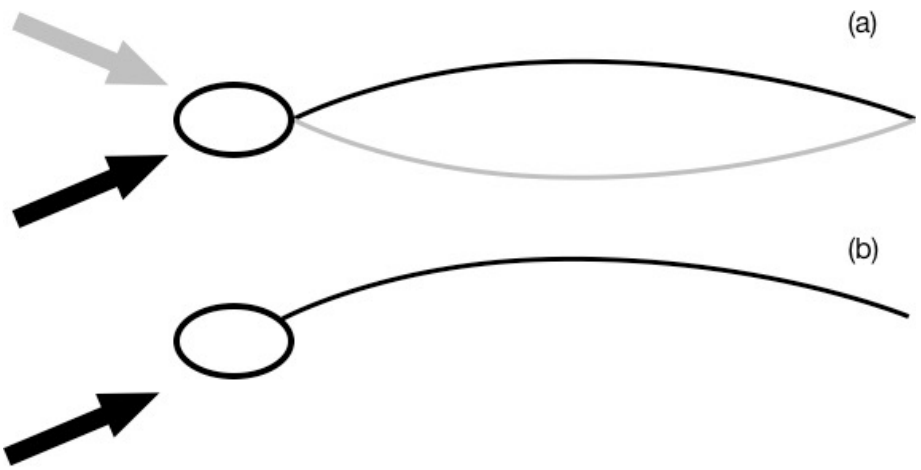


Schematic showing the need for symmetry in a sailboat (a) in which the wind direction can be on either side of the mast, compared to a (pterosaur) wing (b) in which the predominant flow orientation is from one side only.

## Figure 2.2

Pterosaur wing cross section (redrawn from the shape proposed by Padian & Rayner (1993), showing the asymmetric location of the membrane relative to the wing spar and a wedge of soft tissue posterior to the wing spar.

## Figure 2.3

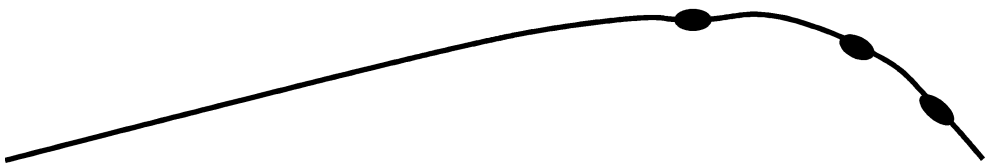

Section through a bat wing, showing position of wing bones relative to the membrane. (From Norberg 1972).

# Figure 2.4

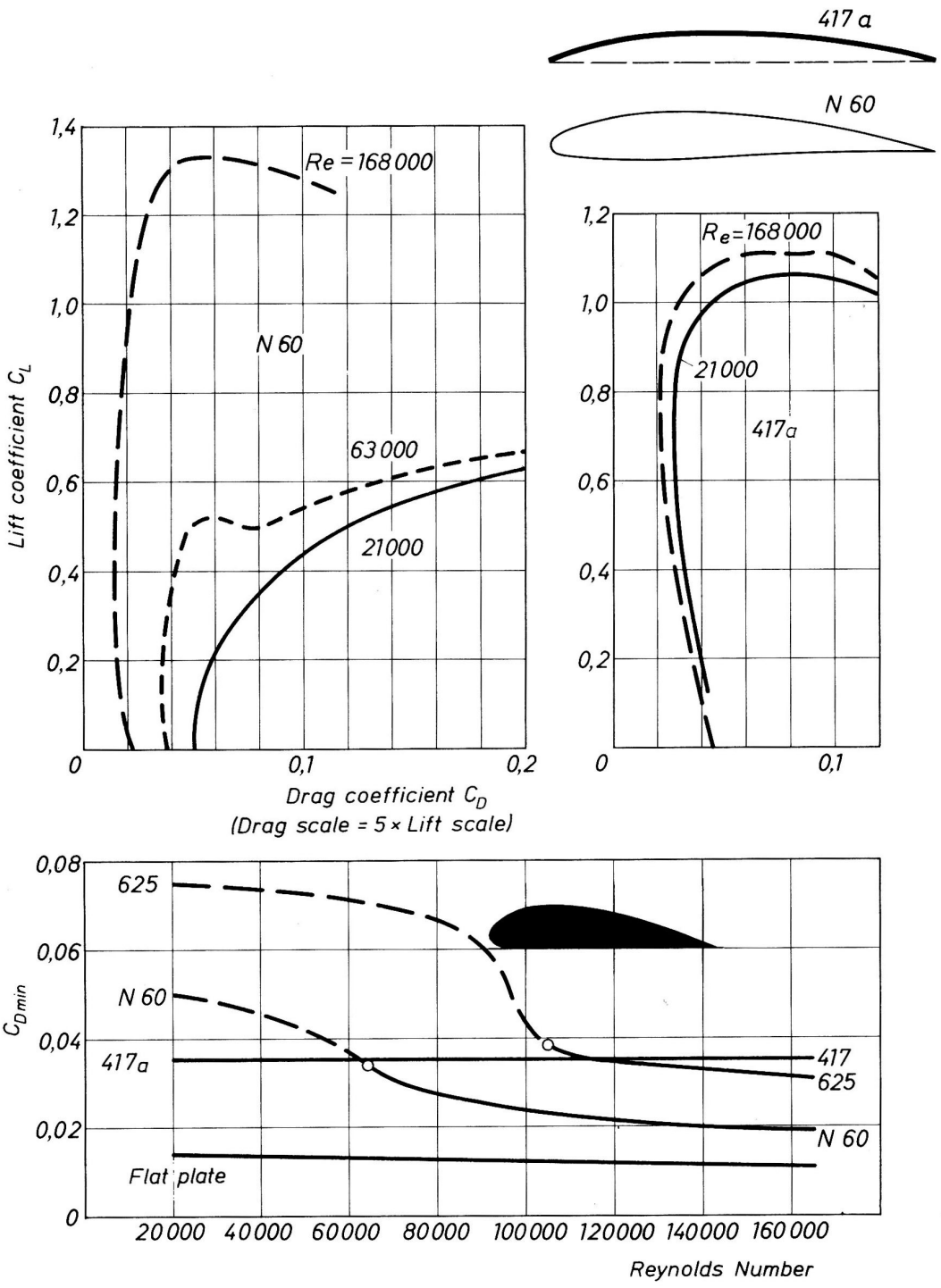


Effect of Reynold's number on the lift and drag of thin and thick airfoil sections. (From Marchaj 1979). The 417a section is a simple cambered plate, the N60 a typical conventional airfoil. At low Reynolds number ($<10^5$) the 417a section can produce a much higher lift coefficient than the thick section.

## Figure 2.5

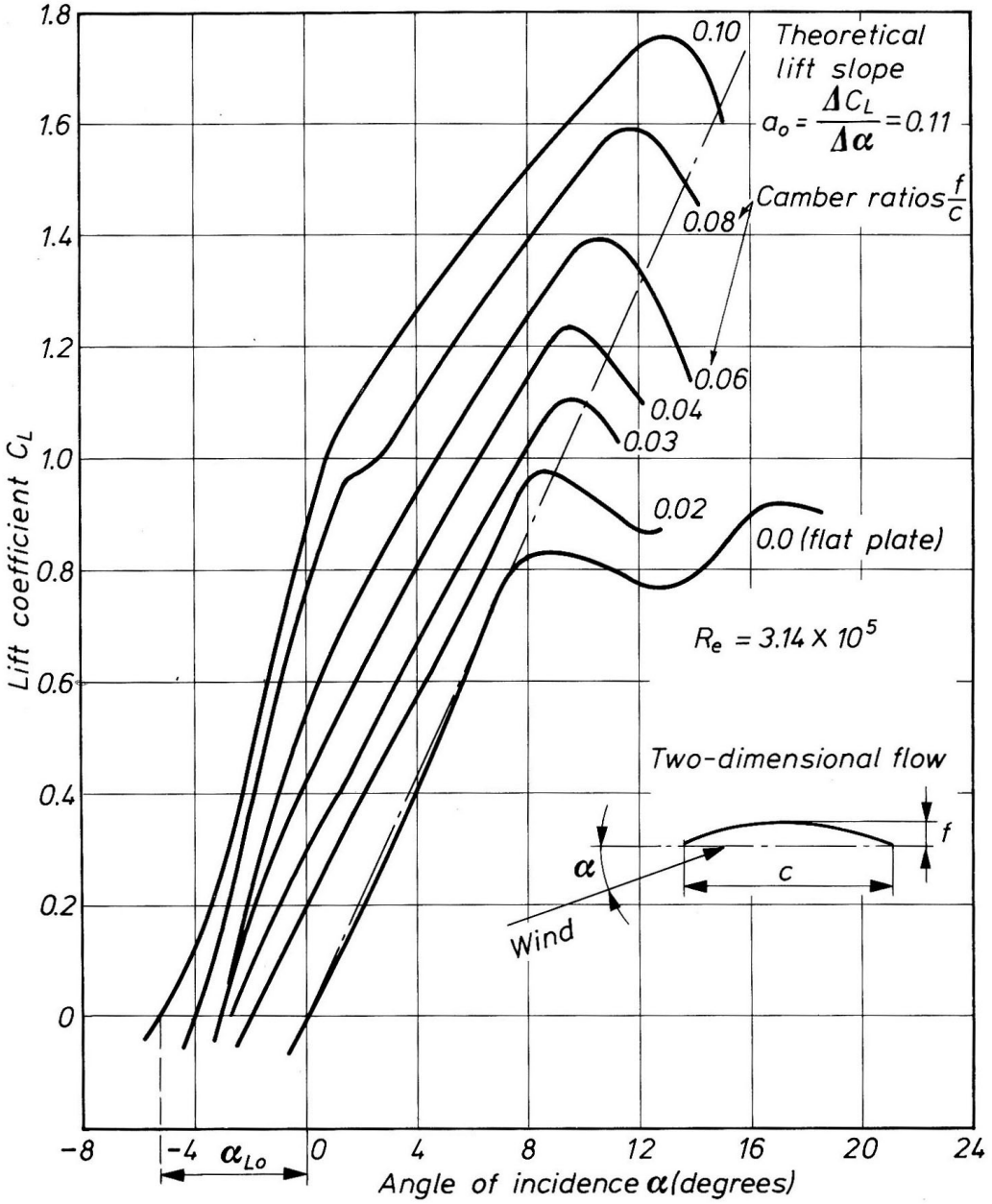


Effect of camber on maximum lift coefficient, showing an approximately linear rate of increase with camber, from 0.9 for a flat plate to almost 1.8 for a curved plate with 10% camber. (From Marchaj 1996).

## Figure 2.6

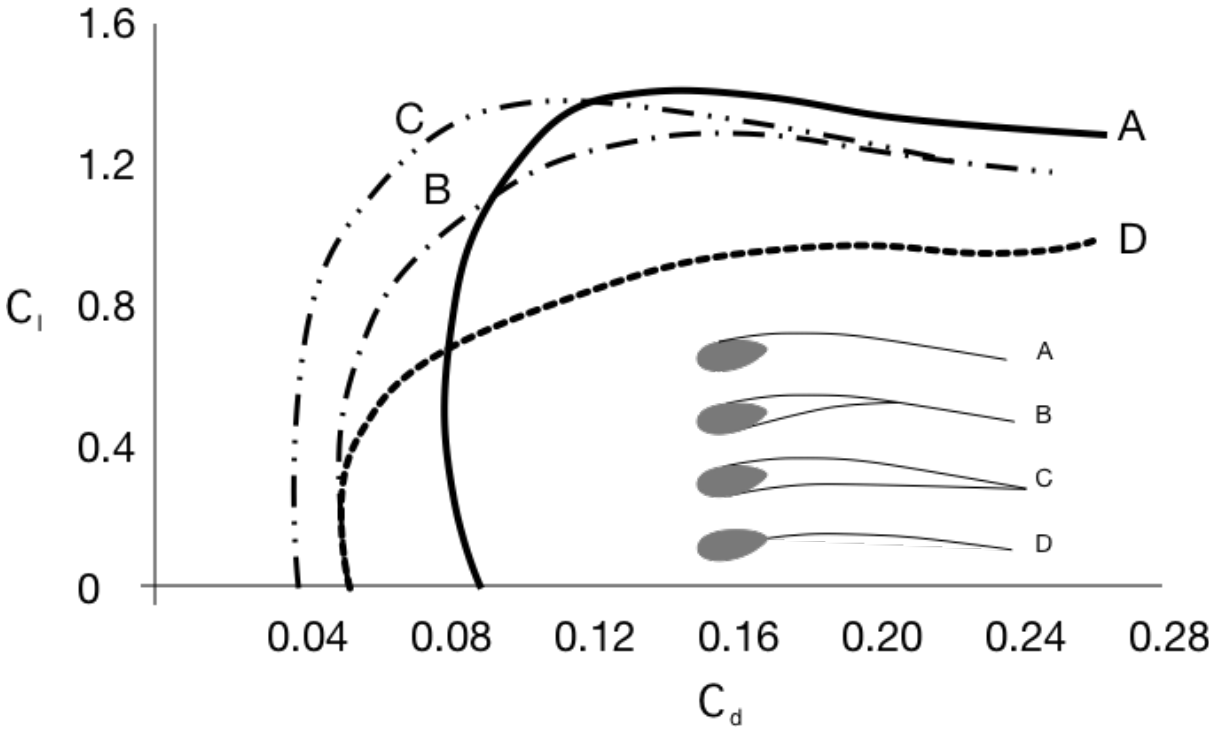


Selected Princeton Wing sailwing sections as tested by Maughmer (1979), (re-drawn from that source.) Comparison of sections A to C shows the effect of fairing behind the wing spar. The maximum lift is effected very little, but the minimum drag is greatly reduced. Sections A and D show the effect of spar position, with a ventral location being clearly superior in terms of maximum lift, but having higher drag.

## Figure 2.7

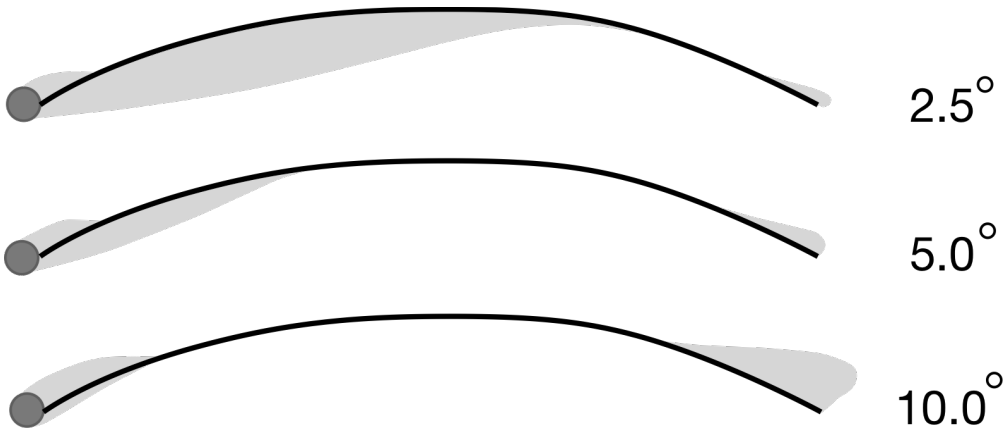


Effect of angle of attack on the size and location of laminar separation bubbles. (From Chaplin *et al.* 2005). The flow direction is from left to right and the shaded areas delineate regions of separated flow. At low angle of attack, there is extensive underside, leading edge separation, but this switches to the other side and to the trailing edge as the angle of attack is increased.

# Figure 2.8

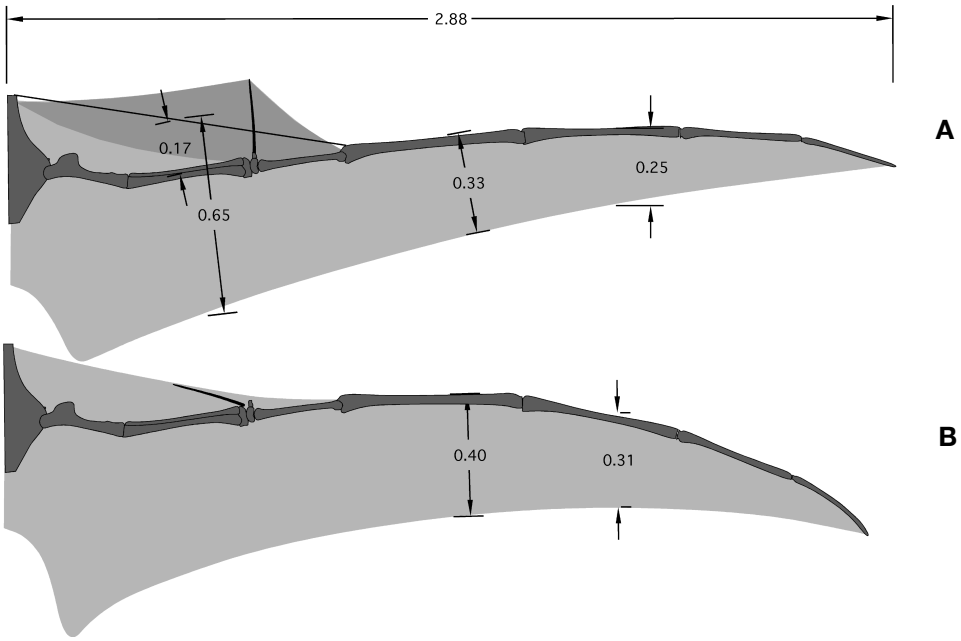


Figure used to estimate the wing section dimensions to be used in the 2D wind tunnel testing. Wing (A) based on Wilkinson (2000) and (B) on Bennett (2001) and Prondvai & Hone (2008). Note that the wide propatagium proposed by Wilkinson *et al.* (2006) was not modelled.

# Figure 2.9

Example of a rigid, 2D wing section model mounted in the wind tunnel. In this case a low camber section fitted with a “WP2” leading edge section.

## Figure 2.10

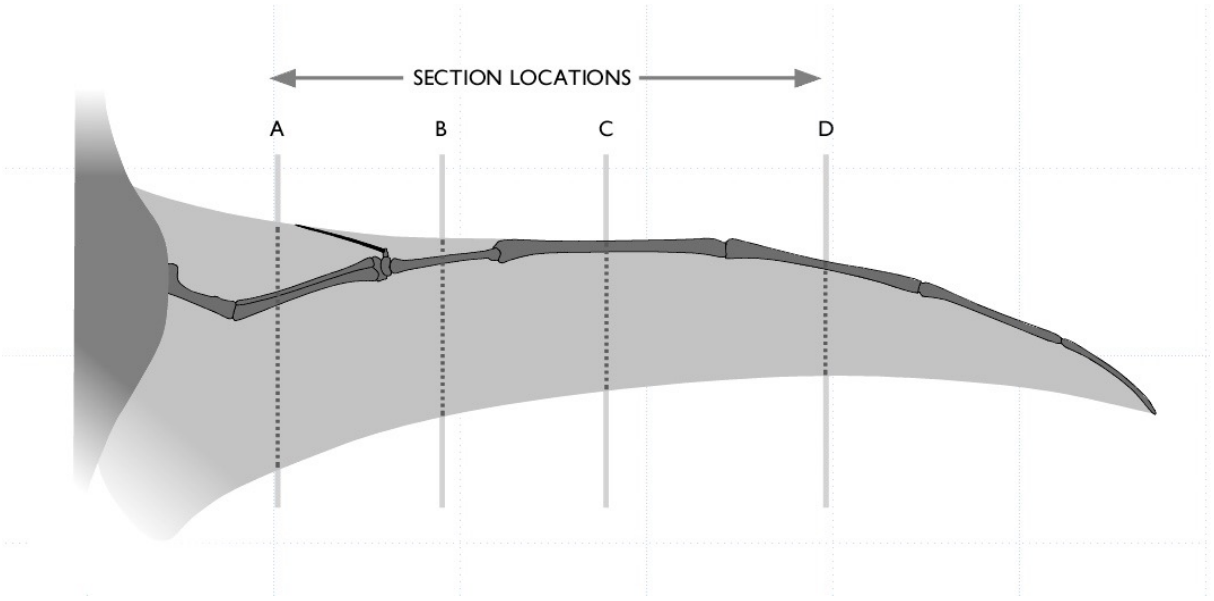


Schematic wing shape showing the locations assumed in the design of the wing sections used in the wind tunnel testing. Location A has a deep propatagium, which is reduced at location B. Locations C and D are at the mid length of the WP1 and WP2 wing phalanges.

## Figure 2.11

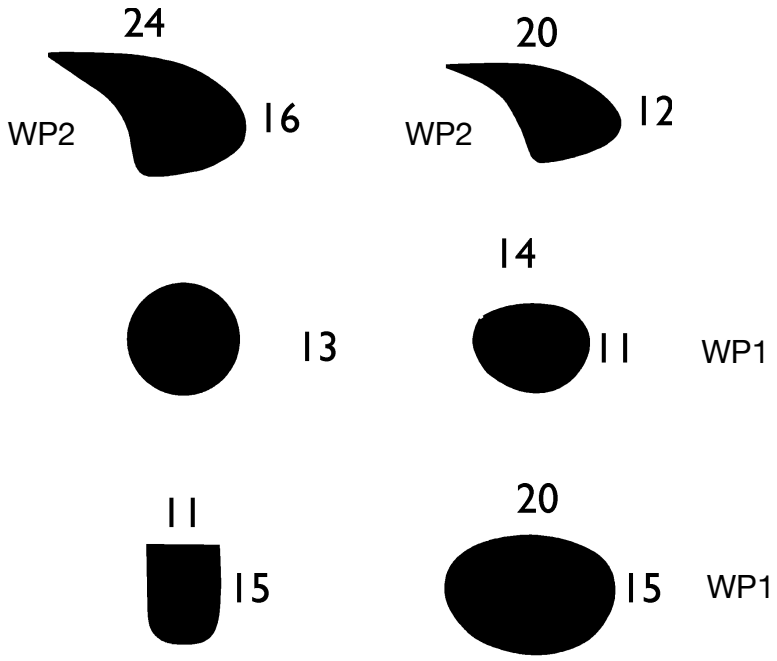


Wing bone cross sections used on wind tunnel models. Numbers are the dimensions in mm.

# Figure 2.12


Flexible wing section, viewed (A) from leading (anterior) edge mounted in the wind tunnel and (B) from the ventral side. Thin black lines running across are the reinforcing threads providing spanwise tensile stiffness, so mimic the action of the aktinofibrils.

# Figure 2.13

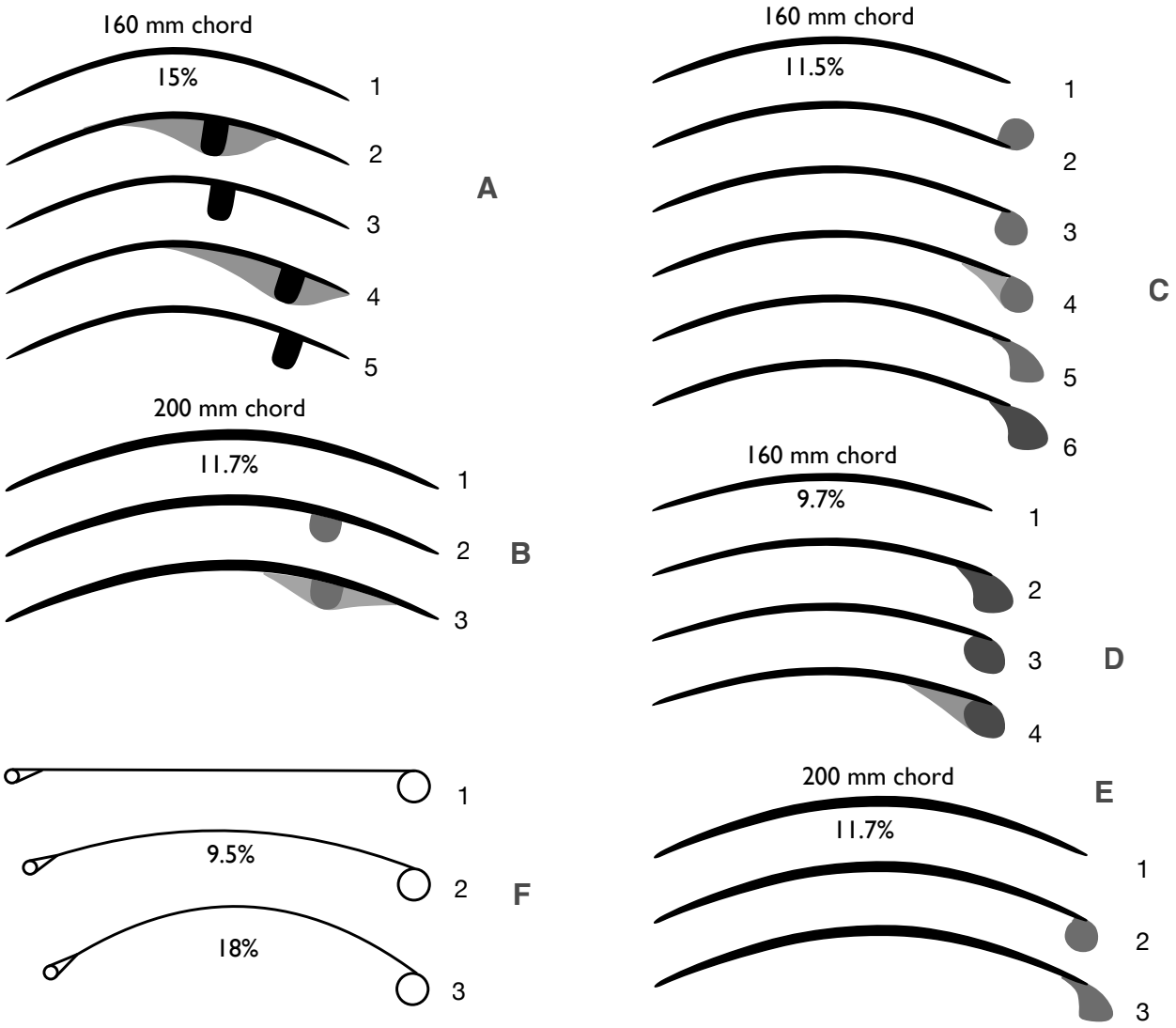


2D wing sections used in wind tunnel testing. Group A sections model the wing at the ulna, with a deep propatagium. Group B are located more distally, across the metacarpal. C, D and E represent the wing finger sections, where the propatagium is absent. The different sections vary the camber, the shape and location of the leading edge wing bone profile and the ratio of bone cross section to chord ratio. Group F are the flexible sections. In cases A to E, a plain section (with no additional wing bones) was also tested in order to provide a reference with published results.

## Figure 2.14

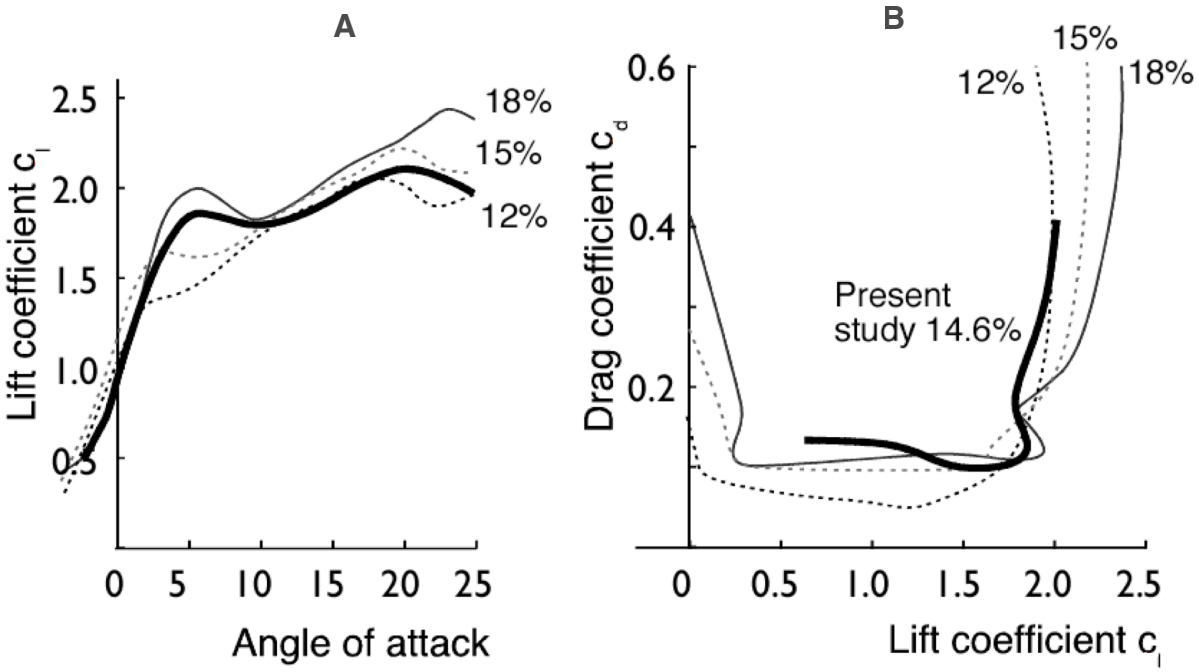


Comparison of present results with those of Milgram (1971). Milgram's (1971) results for camber ratios of 12%, 15% and 18% are shown by thin lines, overlaid with the present result for a camber ratio of 14.6% (heavy line). (A) lift coefficient variation with angle of attack, (B) lift:drag polars.

## Figure 2.15

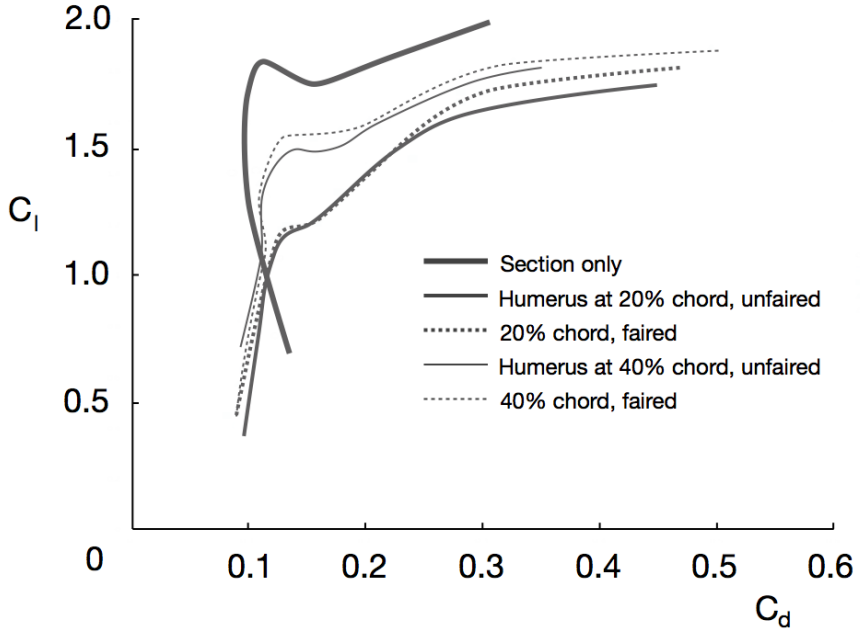


Proximal wing sections showing effect of humerus and extent of propatagium.

## Figure 2.16

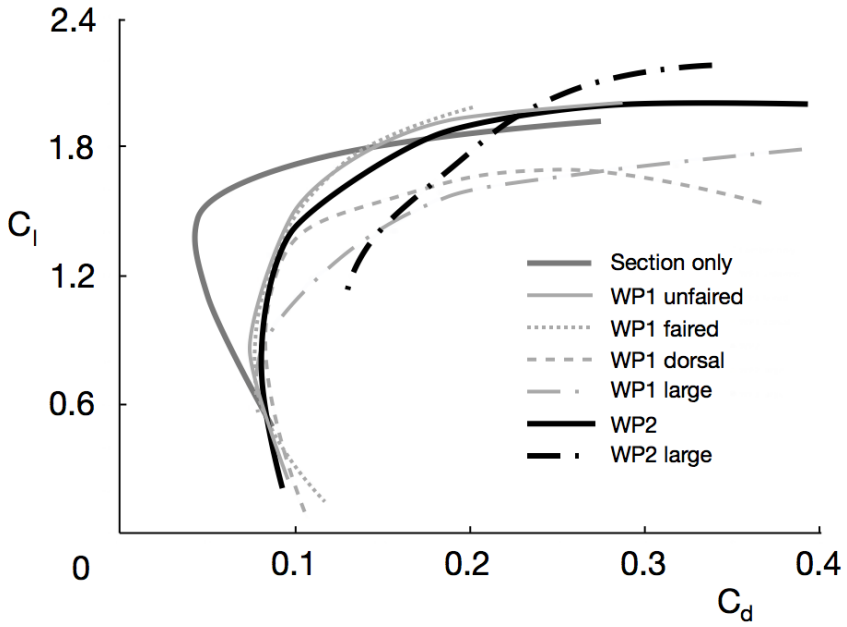


11.6% camber section fitted with different leading edge wing bones (for details of the cross section refer to Figures 2.11 and 2.13). The section with no leading edge bone clearly has the lowest drag and it is apparent that increasing the size of the leading edge section increases drag.

## Figure 2.17

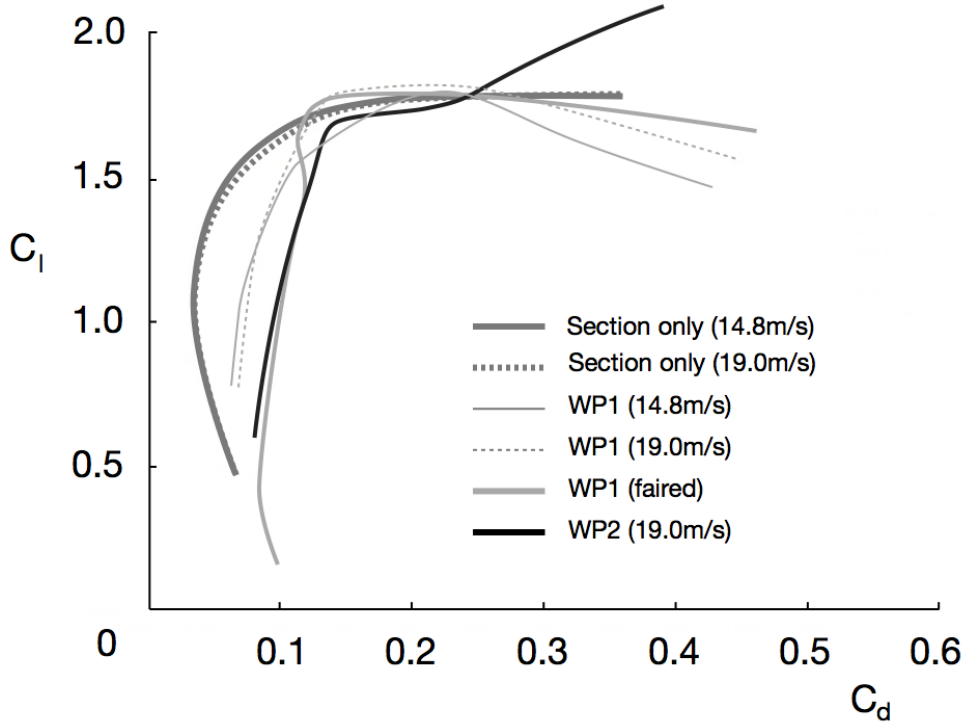


9.7% camber section (representative of distal wing) fitted with different leading edge wing bones. These tests also show the insensitivity to airspeed variation and fairing.

## Figure 2.18

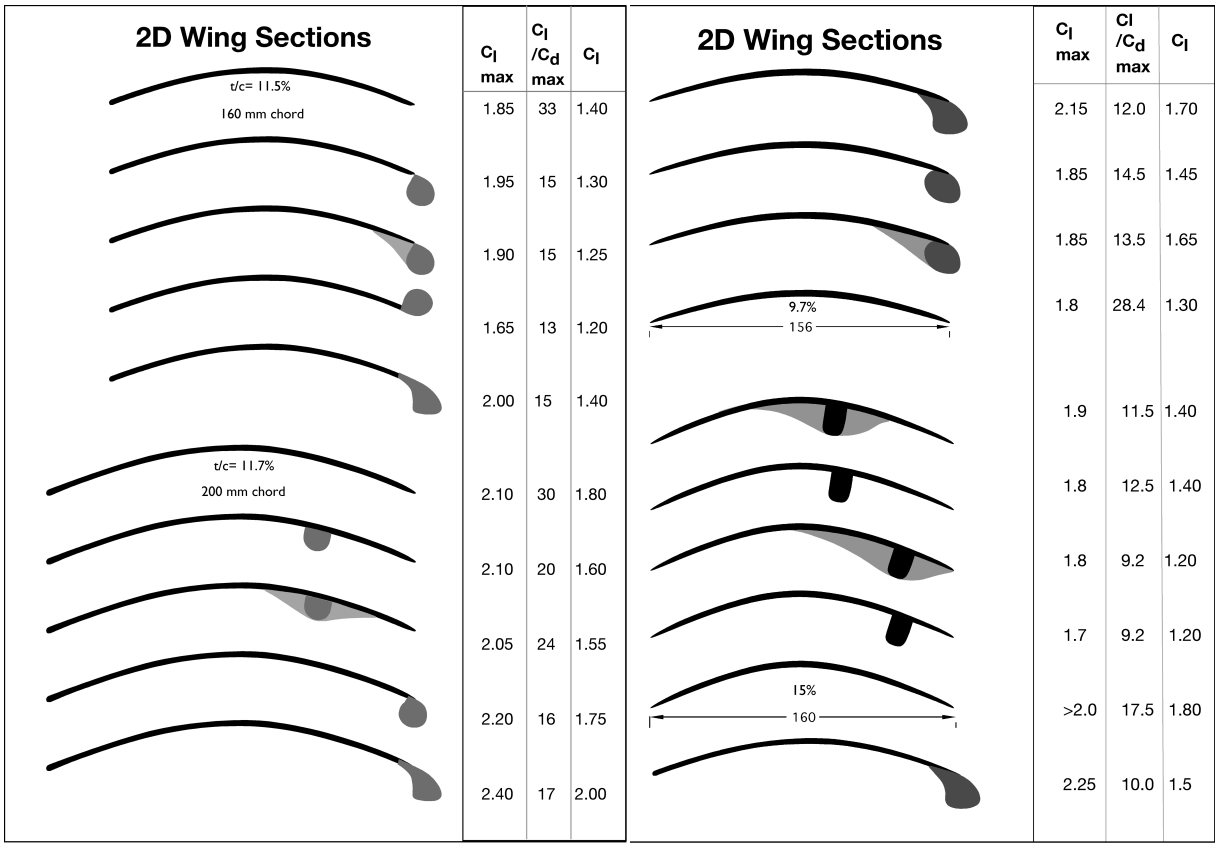


| $C_l$ max | $C_l/C_d$ max | $C_l$ |
|---|---|---|
| 1.85 | 33 | 1.40 |
| 1.95 | 15 | 1.30 |
| 1.90 | 15 | 1.25 |
| 1.65 | 13 | 1.20 |
| 2.00 | 15 | 1.40 |
| 2.10 | 30 | 1.80 |
| 2.10 | 20 | 1.60 |
| 2.05 | 24 | 1.55 |
| 2.20 | 16 | 1.75 |
| 2.40 | 17 | 2.00 |

| $C_l$ max | Cl /$C_d$ max | $C_l$ |
|---|---|---|
| 2.15 | 12.0 | 1.70 |
| 1.85 | 14.5 | 1.45 |
| 1.85 | 13.5 | 1.65 |
| 1.8 | 28.4 | 1.30 |
| 1.9 | 11.5 | 1.40 |
| 1.8 | 12.5 | 1.40 |
| 1.8 | 9.2 | 1.20 |
| 1.7 | 9.2 | 1.20 |
| >2.0 | 17.5 | 1.80 |
| 2.25 | 10.0 | 1.5 |

Summary of aerodynamic characteristics of rigid wing sections. For each wing section the key aerodynamic characteristics are listed - maximum lift coefficient, best lift:drag ratio and the lift coefficient at which this occurs.

## Figure 2.19

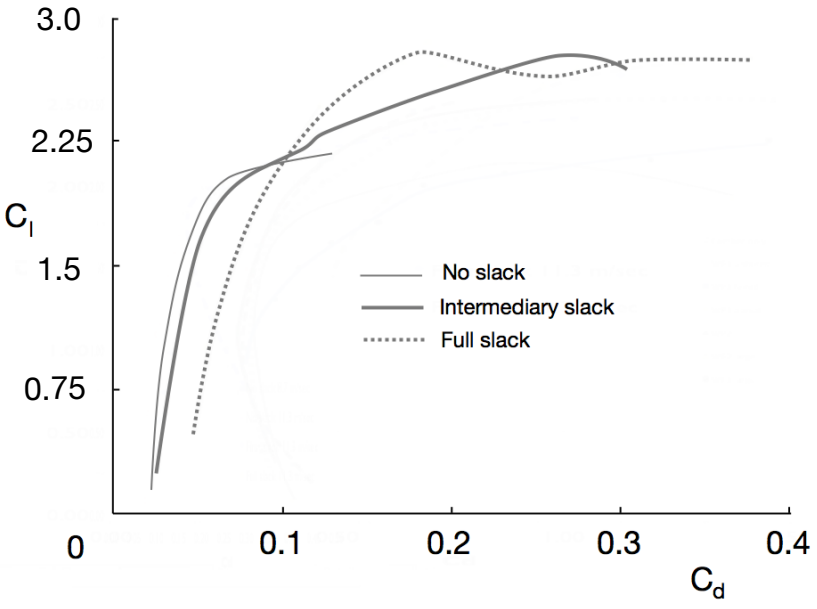


Polar performance of flexible sections at different degrees of membrane slackness (camber). Drag and maximum lift coefficient increase as the camber (membrane slackness) increases.

## Figure 2.20

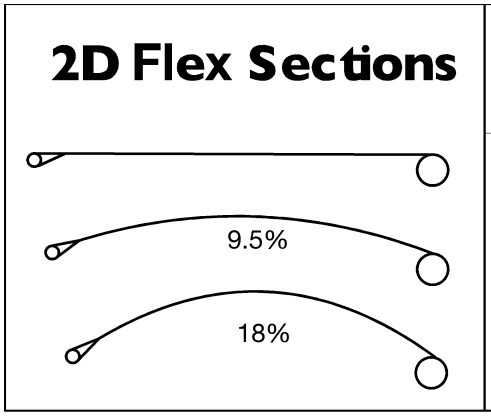


| $C_l$ max | $C_l$ /$C_d$ max | $C_l$ |
|---|---|---|
| 1.95 | 12.5 | 1.25 |
| 2.70 | 9.0 | 1.40 |
| 2.80 | 6.0 | 1.60 |

Summary of aerodynamic characteristics of flexible wing sections (same parameters as in Figure 2.18).

## Figure 2.21

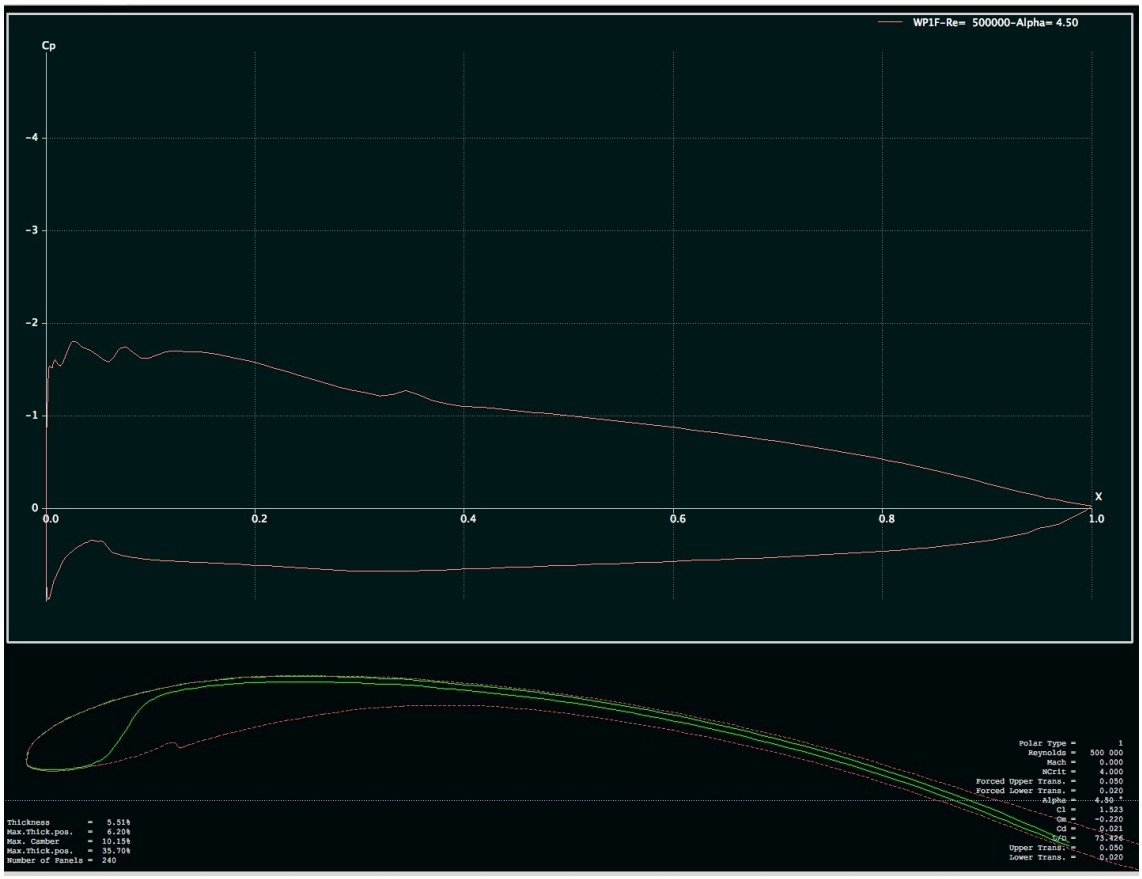


Typical output screen from XFOIL. Upper panel shows pressure distribution and lower panel the outline boundary of the regions of separated flow. Note the large extent of separation posterior to the wing bone.

## Figure 2.22


Effect of fairing on the extent of separated flow, redrawn from a systematic series of XFOIL, and example of which is shown in Figure 2.21. Separated flow is shown by grey shading. As the extent of wing bone fairing increases (A through to D), the extent of undersurface separation decreases.

## Figure 2.23

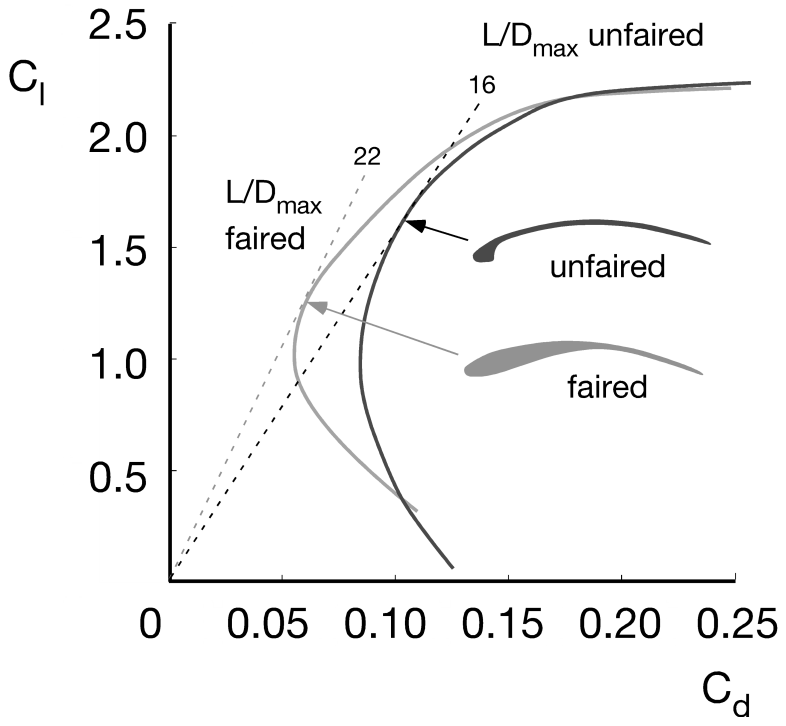


Effect of fairing the wing section in accordance with XFOIL analysis. Minimum drag is reduced by almost 35% and best lift:drag ratio is improved by 27%. $C_{lmax}$ is unchanged.

## Figure 2.24

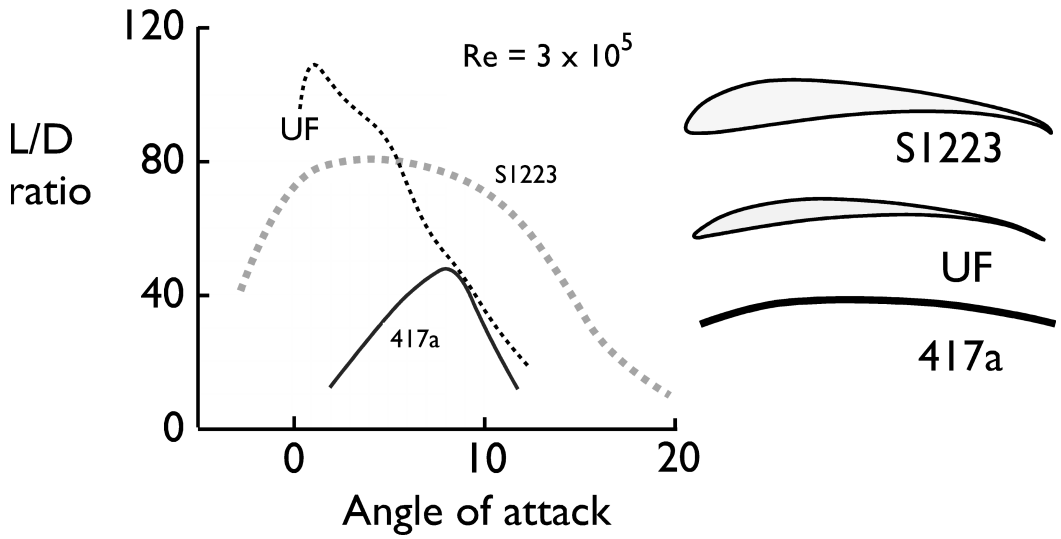


Comparison of aerodynamic efficiency (L/D ratio) of specially developed, low Reynolds number airfoils and a cambered plate section.